Nonlinear Finite Element Analysis of Reinforced Concrete Cylindrical Shells

David A.M.Jawad
Department of Civil Engineering
University of Basrah
College of Engineering

***Abstract*-The study investigates the behavior of reinforced concrete cylindrical shells under monotonically increasing loads. Three-dimensional models of six small-scale experimental shells with length-to-radius ratios ranging from short (0.84) to long (5.0) are implemented within the context of the finite element method, through use of the ANSYS computer code, and the nonlinear response is traced throughout the entire load range up to failure. Cracking occurs at working load levels, with subsequent reduction in shell stiffness. Increasing loads lead to failure modes varying from a beam failure in long shells, combined longitudinal and transverse cracking in intermediate length shells, and abrupt diagonal with limited transverse cracking in short shells. Ultimate load capacities range from 5.0 kPa to 60.0 kPa increasing with decreasing length-to-radius ratios.**

Keywords: Cylindrical shells; reinforced concrete; finite element method; material nonlinearity; ANSYS.

I. Introduction

The cylindrical shell is a singly curved, developable surface, most commonly having a cross section which is a circular arc. The surface is bounded by two straight edges parallel to the axis of the cylinder and by two curved edges in planes perpendicular to the axis. Cylindrical shells may be classified according to their length-to radius ratio as long (l/r>5) or short (l/r<1). In short cylindrical shells, the loads are carried essentially by arch action to the longitudinal edges, where they are transferred to the transverse supports by the edge sections of the shell acting as deep beams. If the cylindrical shell is long, it behaves primarily as a beam of thin curved section, although there is still some arch action near the crown. Short cylindrical shells are used for aircraft hangars and auditoriums. They have been built with transverse spans of about 50-100 m, and with longitudinal spans of 6-16 m between stiffening ribs. Long cylindrical shells are more commonly used for warehouses and factories, where longitudinal spans of about 16-50 m are required, with transverse spans of 6-12 m (Billington,1979) [1].

Reinforced concrete cylindrical shells have traditionally been designed according to either the membrane theory or the bending theory. The membrane theory is based upon the assumption of no bending or transverse shear in the shell and only in-plane forces are considered, whereas bending theory implies a formulation which includes both in-plane and bending forces. A main assumption inherent in both theories is that the shell material is linearly elastic which may be valid at low level working loads. However, for higher load levels and due to the material nonlinearity caused mainly by cracking of the concrete and plasticity of the reinforcement and the concrete; the assumption of linear elastic behaviour is no longer applicable and a nonlinear analysis is required. Several studies on the classical and finite element analysis of reinforced concrete cylindrical shells have been presented; including the works of (Mikkola and Schnobrich 1970, Buyukozoturk 1977, Assan 2002, Suanno et al 2003, Channdrasekaran et al 2009, and Sadowski and Rotter 2013) [2-7].

The objective of this study is to investigate the behaviour of reinforced concrete cylindrical shells at ultimate incorporating material nonlinear finite element analysis. Three dimensional models are developed for six small-scale experimental shells utilizing the ANSYS computer code. The loads are increased gradually up to failure and the resulting stress distributions and crack patterns are investigated for length-to-radius ratios ranging from short (0.84) to long (5.0). Other variables included are edge beam size and reinforcement ratios and arrangements.

II. Governing Equations for Deformation of a Cylindrical Shell

Consider a cylindrical shell with the overall geometry shown in Fig.1. The shell is of length l and thickness h with its axis along the x-direction. The displacements u,v,w correspond to the longitudinal x, circumferential ϕ and radial r directions respectively. Fig.2 shows the differential element considered for analysis.

The three strain components ε_x, ε_ϕ and $\gamma_{x\phi}$ of the middle surface and the three curvature changes χ_x, χ_ϕ, and $\chi_{x\phi}$ can be expressed in terms of the displacement components as:

$$\varepsilon_x = \frac{\partial u}{\partial x}, \quad \varepsilon_\phi = \frac{\partial v}{a\partial\phi} - \frac{w}{a}, \quad \gamma_{x\phi} = \frac{\partial u}{a\partial\phi} + \frac{\partial v}{\partial x},$$

$$\chi_x = \frac{\partial^2 w}{\partial x^2}, \quad \chi_\phi = \frac{1}{a^2}\left(\frac{\partial v}{\partial\phi} + \frac{\partial^2 w}{\partial\phi^2}\right), \quad \chi_{x\phi} = \frac{1}{a}\left(\frac{\partial v}{\partial x} + \frac{\partial^2 w}{\partial x\partial\phi}\right) \quad \text{.....(1)}$$

The resultant forces and moments associated with the above strain components are:

$$N_x = \frac{Eh}{1-\nu^2}(\varepsilon_x + \nu\varepsilon_\phi), \quad N_\phi = \frac{Eh}{1-\nu^2}(\varepsilon_\phi + \nu\varepsilon_x),$$

$$N_{x\phi} = \frac{Eh}{2(1+\nu)}\gamma_{x\phi},$$

$$M_x = -\frac{Eh^3}{12(1-\nu^2)}(\chi_x + \nu\chi_\phi),$$

$$M_\phi = -\frac{Eh^3}{12(1-\nu^2)}(\chi_\phi - \nu\chi_x),$$

$$M_{x\phi} = -M_{\phi x} = \frac{Eh^3}{12(1+\nu)}\chi_{x\phi} \quad \text{.....(2)}$$

Substituting Equations (1) in Equations (2),

$$N_x = \frac{Eh}{1-\nu^2}\left(\frac{\partial u}{\partial x} + \frac{\nu}{a}\left(\frac{\partial v}{\partial \phi} - w\right)\right)$$

$$N_\phi = \frac{Eh}{1-\nu^2}\left[\frac{1}{a}\left(\frac{\partial v}{\partial \phi} - w\right) + \nu\frac{\partial u}{\partial x}\right]$$

$$N_{x\phi} = \frac{Eh}{2(1+\nu)}\left[\frac{\partial u}{a\partial \phi} + \frac{\partial v}{\partial x}\right]$$

$$M_x = \frac{Eh^3}{12(1-\nu^2)}\left[\frac{\partial^2 u}{\partial x^2} + \frac{\nu}{a^2}\left(\frac{\partial v}{\partial \phi} + \frac{\partial^2 w}{\partial \phi^2}\right)\right]$$

$$M_\phi = -\frac{Eh^3}{12(1-\nu^2)}\left[\nu\frac{\partial^2 w}{\partial x^2} + \frac{1}{a^2}\left(\frac{\partial v}{\partial \phi} + \frac{\partial^2 w}{\partial \phi^2}\right)\right]$$

$$M_{x\phi} = \frac{Eh^3}{12(1+\nu)a}\left(\frac{\partial v}{\partial x} + \frac{\partial^2 w}{\partial x\partial \phi}\right) = -M_{\phi x} \quad \text{.....(3)}$$

For small values of the forces N_x, N_ϕ, $N_{x\phi}$ the equations of equilibrium are given by (Timoshenko and W-Krieger, 1970) [8]:

$$a\frac{\partial N_x}{\partial x} + \frac{\partial N_{\phi x}}{\partial \phi} = 0$$

$$\frac{\partial N_\phi}{\partial \phi} + a\frac{\partial N_{x\phi}}{\partial x} - Q_\phi = 0$$

$$a\frac{\partial Q_x}{\partial x} + \frac{\partial Q_\phi}{\partial \phi} + N_\phi + qa = 0$$

$$a\frac{\partial M_{x\phi}}{\partial x} - \frac{\partial M_\phi}{\partial \phi} + aQ_\phi = 0$$

$$\frac{\partial M_{\phi x}}{\partial \phi} + a\frac{\partial M_x}{\partial x} - aQ_x = 0 \quad \text{.....(4)}$$

Eliminating the shearing forces Q_x and Q_ϕ

$$a\frac{\partial N_x}{\partial x} + \frac{\partial N_{\phi x}}{\partial \phi} = 0$$

$$\frac{\partial N_\phi}{\partial \phi} + a\frac{\partial N_{x\phi}}{\partial x} + \frac{\partial M_{x\phi}}{\partial x} - \frac{1}{a}\frac{\partial M\phi}{\partial \phi} = 0$$

$$N_\phi + \frac{\partial^2 M_{\phi x}}{\partial x\partial \phi} + a\frac{\partial^2 M_x}{\partial x^2} - \frac{\partial^2 M_{x\phi}}{\partial x\partial \phi} + \frac{1}{a}\frac{\partial^2 M_\phi}{\partial \phi^2} + qa = 0 \quad \text{.....(5)}$$

Substituting the expressions for forces and moments from Equations (3) into the above equations:

$$\frac{\partial^2 u}{\partial x^2} + \frac{1-\nu}{2a^2}\frac{\partial^2 u}{\partial \phi^2} + \frac{1+\nu}{2a}\frac{\partial^2 v}{\partial x\partial \phi} - \frac{\nu}{a}\frac{\partial w}{\partial x} = 0$$

$$\frac{1+\nu}{2}\frac{\partial^2 u}{\partial x\partial \phi} + a\frac{1-\nu}{2}\frac{\partial^2 v}{\partial x^2} + \frac{1}{a}\frac{\partial^2 v}{\partial \phi^2} - \frac{1}{a}\frac{\partial w}{\partial \phi} + \frac{h^2}{12a}\left(\frac{\partial^3 w}{\partial x^2\partial \phi} + \frac{\partial^3 w}{a^2\partial \phi^3}\right) +$$

$$\frac{h^2}{12a}\left[(1-\nu)\frac{\partial^2 v}{\partial x^2} + \frac{\partial^2 v}{a^2\partial \phi^2}\right] = 0$$

$$\nu\frac{\partial u}{\partial x} + \frac{\partial v}{a\partial \phi} - \frac{w}{a} - \frac{h^2}{12}\left(a\frac{\partial^4 w}{\partial x^4} + \frac{2}{a}\frac{\partial^4 w}{\partial x^2\partial \phi^2} + \frac{\partial^4 w}{a^2\partial \phi^4} -\right.$$

$$\left.\frac{h^2}{12}\left(\frac{2-\nu}{a}\frac{\partial^3 v}{\partial x^2\partial \phi} + \frac{\partial^3 v}{a^3\partial \phi^3}\right)\right) = -\frac{aq(1-\nu^2)}{Eh} \quad \text{.....(6)}$$

The systems of differential equations (6) represent the governing equations for a cylindrical shell subjected to a lateral load.

III. Shell Geometry and Material Properties

The basic geometrical configuration of the small scale shell models tested in (Harris and White 1972) [9] is shown in Fig. 3. The shell geometry has an enclosed angle of 40.5° and a length–to-radius ratio ranging from 0.84 to 5.0. The other major variables are edge beam size and reinforcing percentages and arrangements.

Table 1 gives the dimensions of the six shell models reviewed herein. The specimen terminology denotes the type of shell and the reinforcement used in it: L=long ($l/r \geq 5$); I=intermediate ($5 > l/r \geq 1$); S=short ($l/r < 1$). The last letter (F or C) denotes the reinforcing mesh, either hand fabricated (F) or a commercial woven mesh (C). The thickness "t" for all models is 6.65 mm. The reinforcement patterns for the shells are given in Table 2, and the concrete and reinforcement properties are summarized in Table 3.

IV. Finite Element Models

The cylindrical shells are modeled using the SOLID65 element available to ANSYS, which is an eight-node hexahedral element with three degrees of freedom at each node corresponding to translations in the nodal x, y, and z directions (ANSYS 12.0, 2009) [10]. The element is capable of plastic deformation, cracking in three orthogonal directions, and crushing. The smeared approach is adopted for reinforcement, which assumes that the reinforcement is uniformly spread throughout the concrete elements. The

smeared approach assumes perfect bond between steel and concrete. The validity of perfect bond may be questioned, but the nature of distribution of bond stresses near the contact surface between steel and concrete is not exactly established. To include the effect of bond in a mathematical model is rather difficult because the bond stress is not only a function of slip but in reality depends on such factors as the steel stress, the length of embedment, the strength of concrete and the ratio of steel reinforcement(Valliapan and Doolan 1972) [11]. The SOLID65 element allows three rebar materials in the concrete corresponding to three orthogonal directions in the element, thus the uniaxial stiffness and directional orientation have to be defined for the reinforcement. The three-dimensional discretization of the models is achieved by the "extrusion" facility within the ANSYS software, in which the cross-section of the shell is meshed using two-dimensional elements and the meshed area then used as a pattern and "extruded" along the length of the shell model. The straight edges are free and zero displacements are enforced on the curved edges to account for the end diaphragms which are not included in the finite element models. The loading consists of a uniform pressure applied to the top surface of the shell models. Figs. (4-8) show the finite element models corresponding to the long, intermediate, and short shells considered in this study.

V. Nonlinear Behavior

The nonlinear behavior of a reinforced concrete member can be roughly divided into three intervals: the uncracked elastic stage, crack propagation, and the plastic stage. The nonlinear response is caused by either material or geometrical nonlinearity or a combination of both. The material nonlinearity is caused by two major effects, cracking of the concrete, and plasticity of the reinforcement and the concrete. Geometric nonlinearity is caused by large deformations. Time-dependent effects such as creep, shrinkage, and temperature change also contribute to the nonlinear response. This study considers only time-independent material nonlinearities.

The use of the finite element method to predict the behaviour of reinforced concrete requires a realistic modeling of the properties of the constituent materials. Several models have been proposed to characterize the stress-strain and failure behaviour of concrete material under multi-dimensional stress states; however, all these models have certain inherent advantages and disadvantages which depend to a large extent on their particular application. Reinforcing steel is generally assumed to be capable of transmitting axial force only; therefore a uniaxial stress-strain relationship is sufficient for general use.

Most of the formulations of concrete material models are either elasticity-based or plasticity-based models:

i-Elasticity models: An elastic model is defined to be one for which the stress depends only on the strain and not on the history of that strain. In general, two different approaches are employed in the formulation of nonlinear elastic models. These are the total and the incremental stress-strain models. In the total (secant) stress-strain models, the current state of stress is assumed to be uniquely determined as a function of the current state of strain. The incremental stress-strain models are utilized to describe the behaviour of materials in which the state of stress depends on the current state of strain, and on the stress path followed to reach that state. Elastic formulations can be quite accurate for concrete sustaining proportional loading; however, these formulations fail to identify inelastic deformations.

ii-Plasticity models: The basis for the application of plasticity theory to concrete is the assumption that non-recoverable deformations in concrete can be described in the same manner as metals. In general, models based on the theory of plasticity describe concrete as an elastic-perfectly plastic material or an elastic-strain hardening plastic material. For the first approach it is assumed that the stress-strain relationships include three parts: before yielding, during plastic flow, and after fracture. Concrete behaviour before yielding is assumed to be elastic; linear or nonlinear elasticity based models are used to characterize the behaviour in this region. During plastic flow, the behaviour of concrete is described by the plastic stress-strain relations. Post fracture behaviour is governed by the constitutive relations of fracture. In most practical applications, concrete after crushing is assumed to lose its resistance completely against further deformations and the current stresses (just before crushing) drop suddenly to zero.

The elastic-strain hardening approach is based on the existence of an initial yield surface and the evolution of subsequent loading surfaces. The initial yield surface is the limiting surface for elastic behaviour. When the material is stressed beyond the initial yield surface, a subsequent new yield surface called the loading surface is developed; this new surface replaces the initial yielding. Unloading and reloading of the material within this subsequent loading surface results in elastic behaviour, and no additional irrecoverable deformation will occur until this new surface is reached. Further loading surfaces and additional irrecoverable plastic deformation will result if loading is continued beyond this surface. Final collapse of the concrete occurs when the fracture surface is reached and concrete cracking or crushing takes place, depending on the nature of the stress state. The formulation of a stress-strain relationship for a strain-hardening plastic material is based on three fundamental assumptions: shape of the initial yield surface, evolution of subsequent loading surfaces (hardening rule), and the formulation of an appropriate flow rule which specifies the stress-strain relation in the plastic range. Furthermore, the total strain increment vector is assumed to be the sum of the elastic and plastic strain components.

VI. Material Idealization

Concrete behavior is simulated by the elastic-plastic model with a five-parameter William-Warnke failure surface[12]. The failure surface consists of a conical shape with curved meridians and non-circular base sections; it is defined as:

$$\frac{1}{z}\frac{\sigma_a}{f_{cu}} + \frac{1}{r(\theta)}\frac{\tau_a}{f_{cu}} = 1 \quad \cdots\cdots(7)$$

Where: σ_a and τ_a are the average stress components, r is the position vector locating the surface with angle θ, z is the apex of the surface and f_{cu} is the uniaxial compressive strength. The free parameters of the surface z and r are

identified from the uniaxial compressive strength f_{cu}, biaxial compressive strength f_{cb} and uniaxial tensile strength f_t. The William-Warnke failure surface has several advantages which include: close fit of experimental data in the operating range; simple identification of model parameters from standard test data; smoothness and convexity (Chen 1982) [13].

In order to guide the expansion of the yield surface during plastic deformation, the uniaxial stress-strain relationship for normal-strength concrete is defined as (MacGregor 1992) [14]:

$$\sigma_c = \frac{E_c \varepsilon_c}{1+\left(\frac{\varepsilon_c}{\varepsilon_0}\right)^2} \quad \cdots(8)$$

$$\varepsilon_0 = \frac{2 f_c'}{E_c} \quad \cdots(9)$$

$$E_c = \frac{\sigma_c}{\varepsilon_c} \quad \cdots(10)$$

Where σ_c = stress at any strain ε, ε_c = strain at stress σ, ε_0 = strain at the ultimate compressive strength f_c'.

The uniaxial stress-strain relationship (8) is approximated by several piecewise linear segments, Fig.9, and the resulting sets of points are incorporated in the material model for concrete.

The modulus of elasticity for concrete is evaluated from

$$E_c = 4730\sqrt{f_c'} \quad \cdots(11)$$

and the uniaxial tensile strength is determined from

$$f_t = 0.62\sqrt{f_c'} \quad \cdots(12)$$

Poisson's ratio is taken as 0.20, and the shear transfer coefficient β_t which represents conditions of the crack face is taken equal to 0.3.

The steel for the finite element models is idealised as an elastic-perfectly plastic material with a modulus of elasticity equal to 207 GPa and Poisson ratio 0.30. The yield strength and ultimate strength are indicated in Table 3.

VII. Results and Discussion

In this section the load-deflection behaviour up to failure is investigated and compared with experimental results for each of the six shell models under consideration. Also reviewed are the longitudinal stress distribution and crack pattern at collapse.

i-Long shell LC-1

The deflection behavior of shell LC-1 as it is loaded to failure is shown in Fig.10. The cracking load equals 2.0 kPa. The continued cracking of the shell results in a gradual loss of stiffness and the shell attains its ultimate load of 5.0 kPa with a midspan deflection of 21.7mm. The discrepancy with the experimental results may be attributed to micro-cracking of concrete and the assumption of perfect bond between steel and concrete. The relatively low gradient of the load-deflection curve as it approaches ultimate results in a larger area under the curve, thus indicating greater energy absorption capacity; hence higher ductility before failure. Fig.11 gives the distribution of longitudinal stresses at failure and indicates a stress concentration at the support region of the edge beams. The shell fails in a beam mechanism as shown in the transverse crack pattern of Fig.12.

ii-Intermediate shells IF-3 and IF-4

Shells IF-3 and IF-4 are identical except for reinforcement; IF-3 has transverse and longitudinal steel in both faces of the shell, while IF-4 has a single mesh in the shell middle surface with a very low percentage in the transverse direction. The load-deflection behaviour is shown in Fig.s. 13 and 14. The cracking load equals 4.0 kPa for both shells. The decrease in stiffness due to cracking is more gradual in IF-3 than for IF-4, but both models show less ductile behviour than the long shell model LC-1 discussed in the previous section. The load and midspan values at collapse are given as 12.0 kPa, 11.16 mm for IF-3, and 8.0 kPa, 4.02 mm for IF-4. The distribution of longitudinal stresses, Fig.s. 15 and 16 also indicate a stress concentration at similar locations to those of model LC-1. The crack patterns at failure in Fig.s. 17 and 18 reveal longitudinal cracking along the centerline of the shells in addition to transverse cracking which may be attributed to the increase of lateral moments.

iii-Intermediate shell IC-2

This shell is half as long as the other intermediate length shells. The load deflection behaviour is shown in Fig.19. The cracking load equals 10.0 kPa and the shell fails at a load of 27.0 kPa with a midspan deflection equal to 1.07 mm. The stress distribution is given in Fig.20. The crack pattern at failure, Fig.21, shows the formation of a diagonal or shear cracking mode in addition to the longitudinal cracking mode which appears in shells IF-3 and IF-4.

iv-Short shells SC-3 and SC-4

The short shell models SC-3 and SC-4 represent models with shallow and deep edge members, respectively. The load-deflection plots for both models, Fig.s. 22 and 23 show a high stiffness gradient thus exhibiting a more brittle mode of failure than the previously discussed models. The cracking load is 20.0 kPa in each of the models which fail at an ultimate load of 60.0 kPa with corresponding deflections equal to 0.62 mm and 0.35 mm for SC-3 and SC-4 respectively. The deviation from experimental results in Fig.22 may be due to micro cracking of concrete and the assumption of perfect bond. The very low deflection values indicate a sudden failure with little or no prior warning in this type of shells. The stress distribution is shown in Fig.s. 24 and 25. The shells exhibit diagonal shear failure cracking patterns at collapse, Fig.s. 26 and 27, with no longitudinal cracking along the centerline, and limited transverse cracking in SC-3.

VIII. Conclusions

- The validity of finite element analysis with ANSYS of reinforced concrete cylindrical shell behaviour is substantiated by comparisons made with small scale experimental models. The general trend of the load-deflection histories followed experimental results well, despite some discrepancies.
- Cracking generally commences at the working load level with a consequent reduction in stiffness, and shell deflections at this stage may be greater than those indicated by a linear elastic analysis. Therefore, care must be taken in computing deflections at working loads; as even a single overload occurrence may cause cracking in the structure.
- The ultimate load capacity of the reinforced concrete shell models increases with decreasing *l/r* ratios. However, short shells demonstrate a much less ductile type of behaviour than is the case for long shells.
- Three distinct cracking patterns are identified at failure as the shell models transition from long to short. The long shell model exhibits transverse crack patterns in a beam mechanism failure mode. The intermediate shell models demonstrate longitudinal cracks in addition to the transverse cracks. The short shell models show diagonal cracking in a shear failure mode.

IX. References

[1] **Billington, D.P. 1979.** Thin-shell structures. In: Gaylord, E. and Gaylord, C., Structural Engineering Handbook, Sec. 20, McGraw-Hill Inc.

[2] **Mikkola, M.J., and Schnobrich, W.C. 1970.** Material behaviour characteristics for reinforced concrete shells stressed beyond the elastic range. Technical Report, University of Illinois.

[3] **Buyukozoturk,O. 1977.** Nonlinear analysis of reinforced concrete structures. Computers and Structures, Vol.7, pp.149-156.

[4] **Assan, A.E. 2002.** Nonlinear analysis of reinforced concrete cylindrical shells. Computers and Structures, Vol.80, pp.2177-2184.

[5] **Suanno, R., Ferrari, L., and Prates, C. 2003.** Nonlinear analysis of concrete shells subjected to impact loads. Transactions of the 17th International Conference on Structural Mechanics in Reactor Technology. Prague, Paper No. J03-1.

[6] **Chandrasekaran, S., Gupta, S.K., and Carannante F. 2009**. Design aids for fixed support reinforced concrete cylindrical shells under uniformly distributed loads. International Journal of Engineering Science and Technology, Vol.1, No.1, pp.148-171.

[7] **Sadowski, A.J., and Rotter, J.M. 2013.** Solid or shell finite elements to model thick cylindrical tubes and shells under global bending. International Journal of Mechanical Sciences, 74, pp.143-153.

[8] **Timoshenko, S., and Woinowsky-Krieger, S. 1970.** Theory of plates and shells. McGraw-Hill Kogakusha.

[9] **Harris, H.G., and White, R.N. 1972.** Inelastic behaviour of R/C cylindrical shells. Journal of the Structural Division, ASCE, Vol.98, No.ST7, Proc. Paper 9074.

[10] **ANSYS 12.0. 2009.** Finite element analysis system, SAS IP, Inc.

[11] **Valliapan, S., and Doolan, T.F., 1972.** Nonlinear Stress Analysis of Reinforced Concrete. Journal of the Structural Division, ASCE, Vol.98, No.ST4, Proc. Paper 8845.

[12] **William, K.J., and Warnke, E.P. 1974.** Constitutive Model for the Triaxial Behaviour of Concrete. Proceed. IABSE Seminar on Concrete Structures subjected to Triaxial Stresses, Bergamo.

[13] **Chen, W.F. 1982.** Plasticity in reinforced concrete. McGraw-Hill Inc.

[14] **MacGregor, J.G. 1992.** Reinforced concrete mechanics and design. Prentice-Hall Inc., Englewood Cliffs, NJ.

Table I Dimensions of six model shells

Mark	Length,*l*, (mm)	Span,S (mm)	Radius,*r* (mm)	*l/r*	Edge beam cross section (mm)
LC-1	1676	434	333	5.0	6.65x33.27
IF-3	1118	434	333	3.35	6.65x33.27
IF-4	1118	434	333	3.35	6.65x33.27
IC-2	559	434	333	1.68	6.65x33.27
SC-3	279	434	333	0.84	6.65x9.53
SC-4	279	434	333	0.84	6.65x33.27

Table II Shell reinforcement

Shell	Bottom surface		Middle surface		Top surface	
	Transverse	Longitudinal	Transverse	Longitudinal	Transverse	Longitudinal
LC-1	-	-	0.43mm @3.18mm	0.43mm @3.18mm	-	-
IF-3	3.25mm @12.7mm	3.25mm @12.7mm	Corner diagonal steel		3.25mm @12.7mm	3.25mm @12.7mm
IF-4	-	-	3.25 @38.1mm	3.25 @12.7mm	-	-
IC-2	-	-	0.43mm @3.18mm	0.43mm @3.18mm	-	-
SC-3			0.43mm @3.18mm	0.43mm @3.18mm	-	-
SC-4			0.43mm @3.18mm	0.43mm @3.18mm	-	-

Table III Material properties and reinforcement ratios

Shell	f'_c (MPa)	Shell reinforcement			Edge beam reinforcement		
		ρ (%)	f_y (MPa)	f_u (MPa)	ρ (%)	f_y (MPa)	f_u (MPa)
LC-1	31.72	1.5	317	379	9.0	317	-
IF-3	28.96	0.94T 0.47B	250	-	5.6	365	400
IF-4	31.17	0.176	275	-	5.6	365	400
IC-2	32.96	1.5	317	379	1.96	300	-
SC-3	38.82	1.5	317	379	2.34	300	-
SC-4	38.82	1.5	317	379	1.35	317	379

f'_c - Compressive strength of concrete

ρ - Ratio of shell reinforcement

f_y - Yield strength of reinforcement

f_u - Ultimate strength of reinforcement

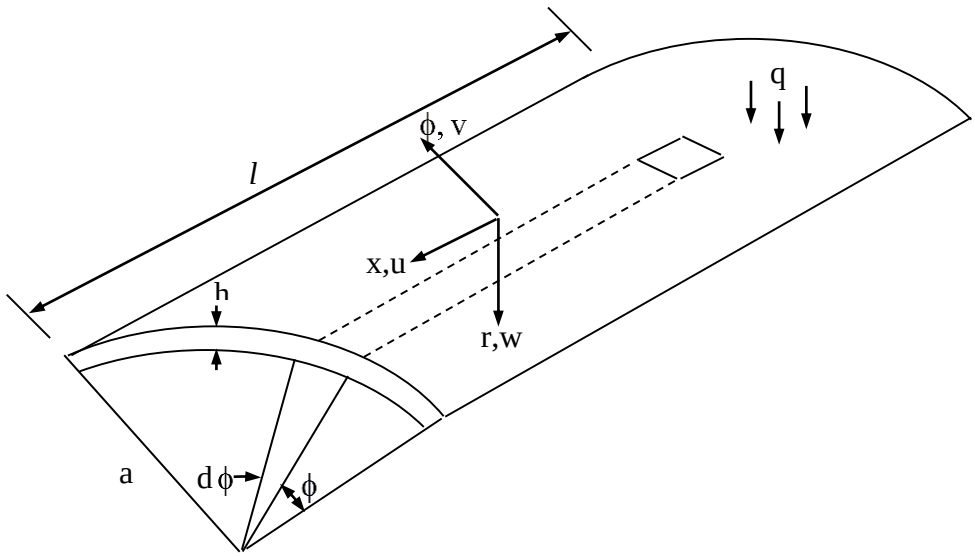

Fig. 1 Overall Geometry

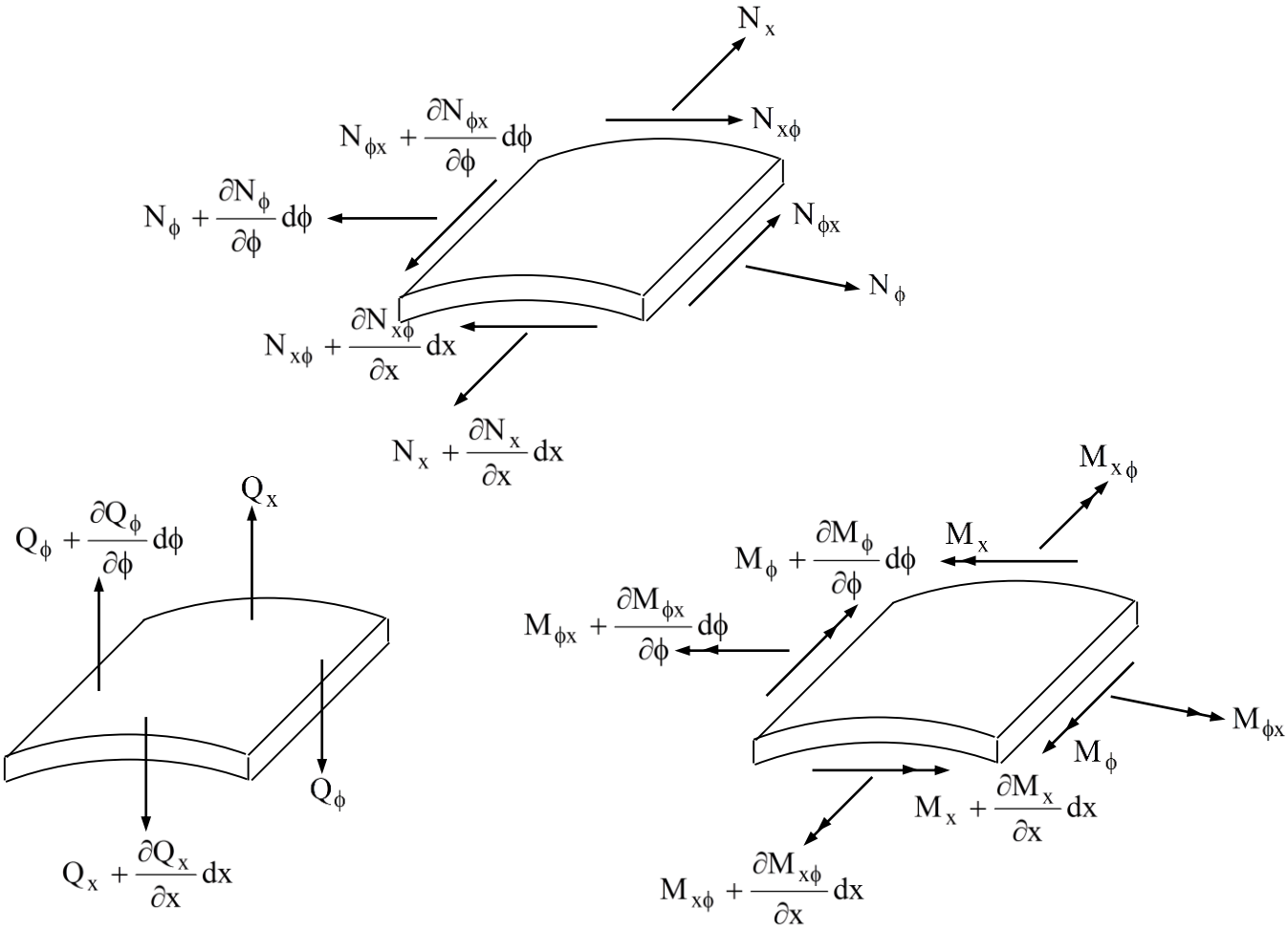

Fig. 2 Differential Element

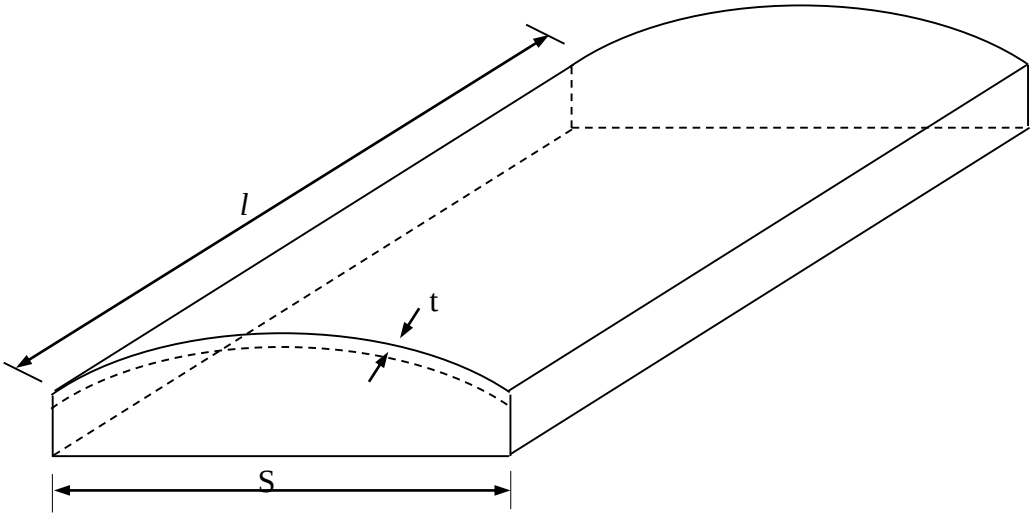

Fig. 3 Experimental Shell Model Geometry

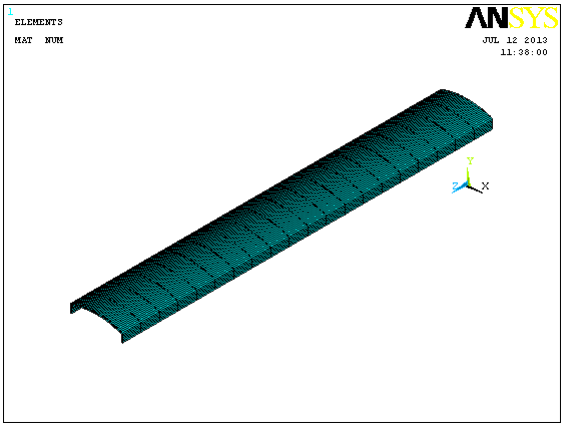

Fig. 4 Finite element shell model LC-1

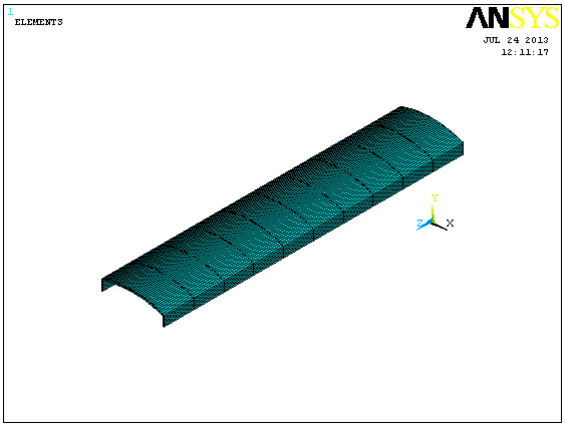

Fig. 5 Finite element shell models IF-3, IF-4

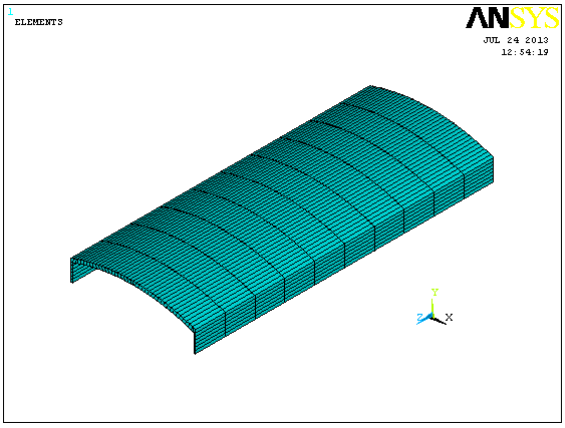

Fig. 6 Finite element shell model IC-2

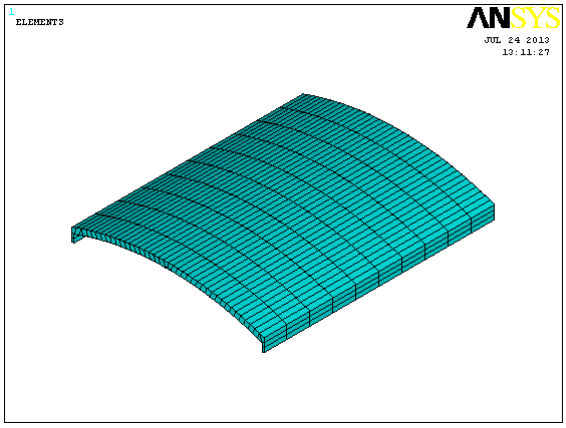

Fig. 7 Finite element shell model SC-3

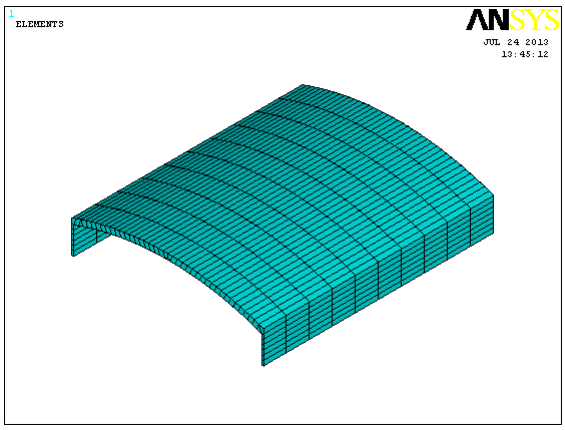

Fig. 8 Finite element shell model SC-4

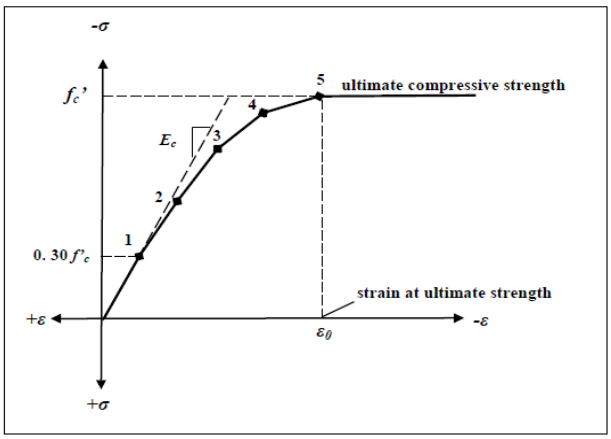

Fig. 9 Adopted stress-strain curve for concrete

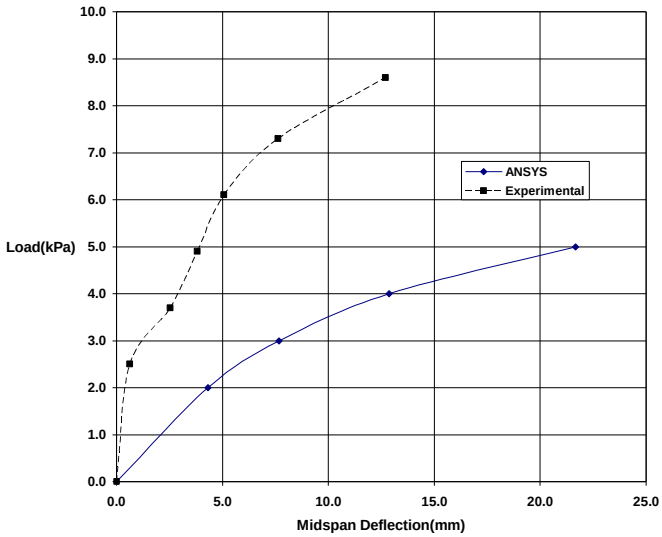

Fig. 10 Load-deflection curve for shell LC-1

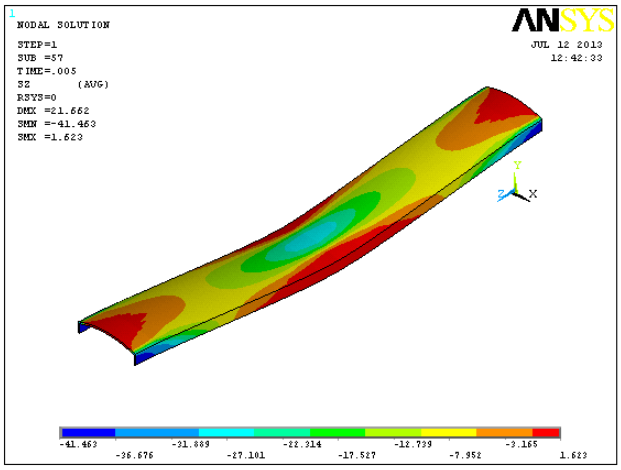

Fig. 11 Longitudinal stress distribution for shell LC-1

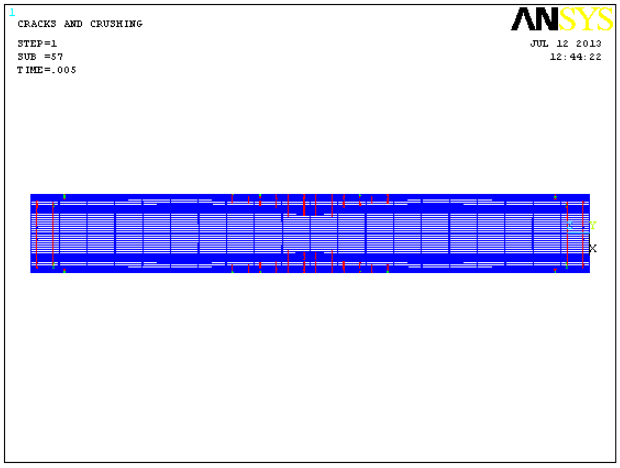

Fig. 12 Crack pattern at failure (top surface) for shell LC-1

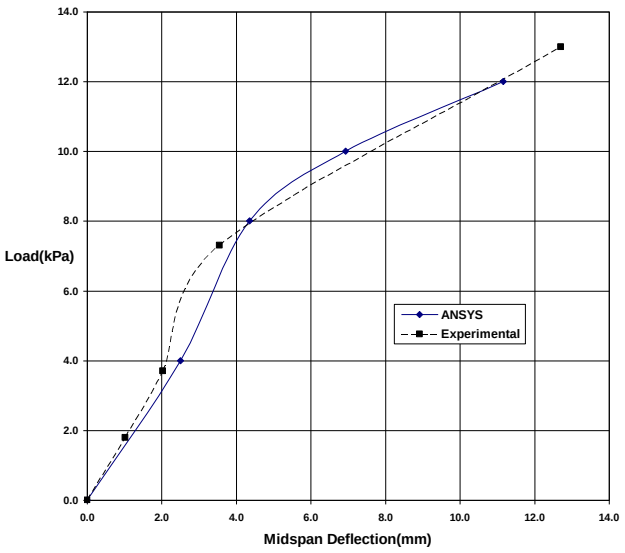

Fig. 13 Load-deflection curve for shell IF-3

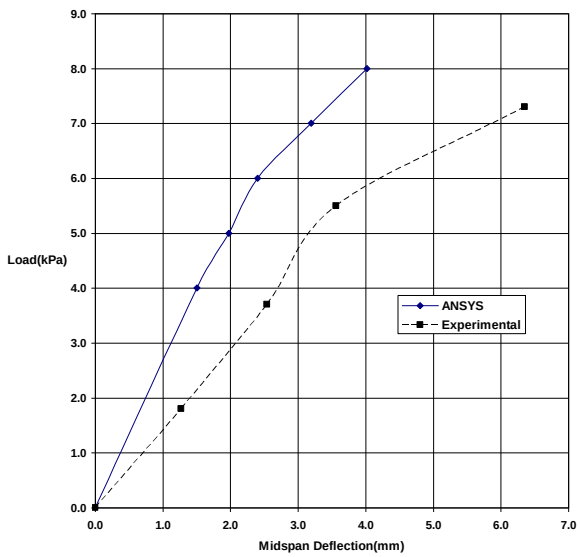

Fig. 14 Load-deflection curve for shell IF-4

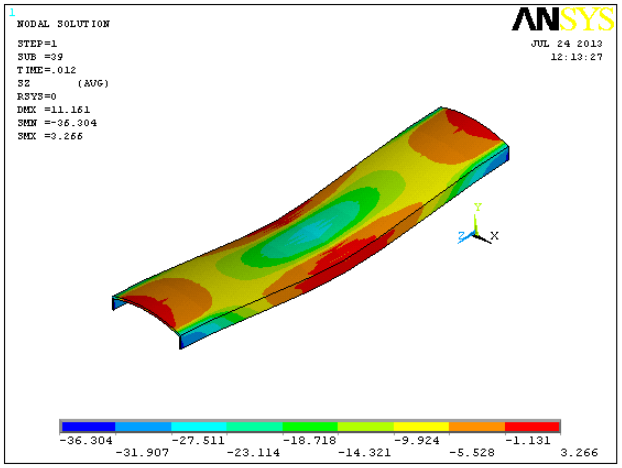

Fig. 15 Longitudinal stress distribution for shell IF-3

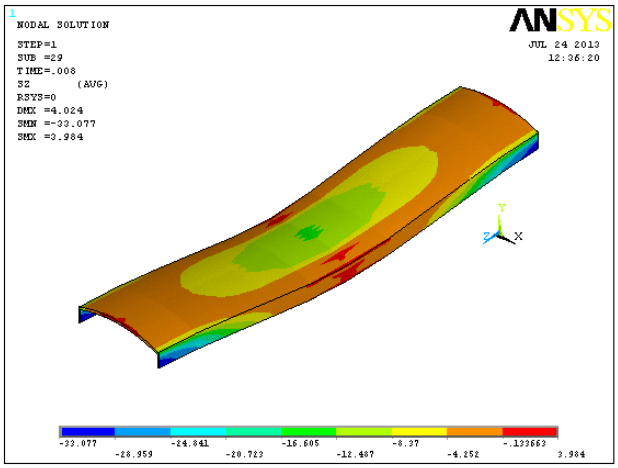

Fig. 16 Longitudinal stress distribution for shell IF-4

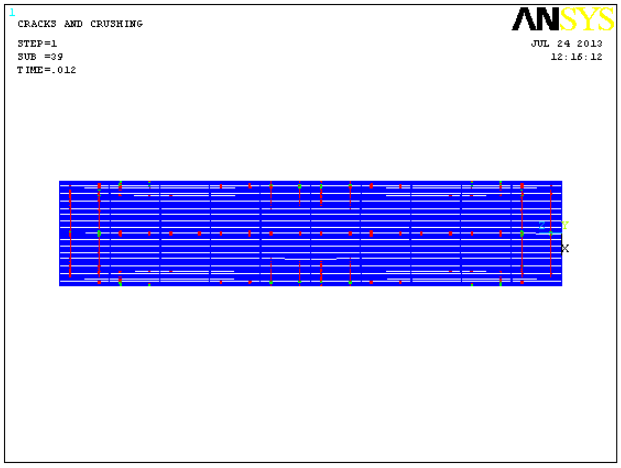

Fig. 17 Crack pattern at failure (top surface) for shell IF-3

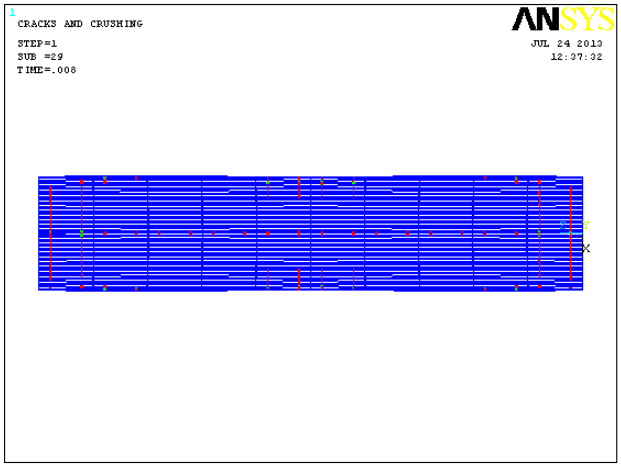

Fig. 18 Crack pattern at failure (top surface) for shell IF-4

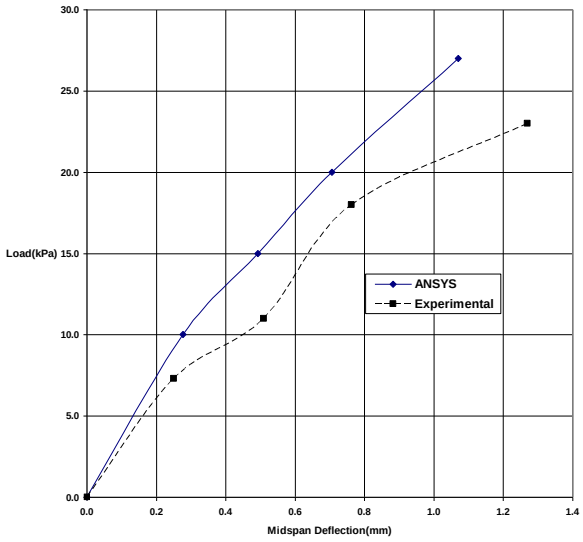

Fig. 19 Load-deflection curve for shell IC-2

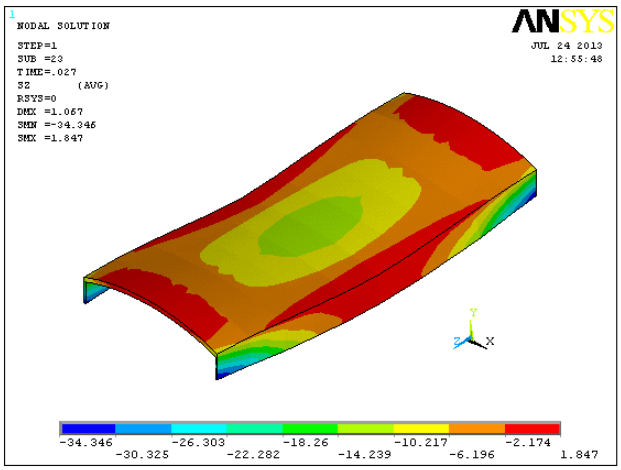

Fig. 20 Longitudinal stress distribution for shell IC-2

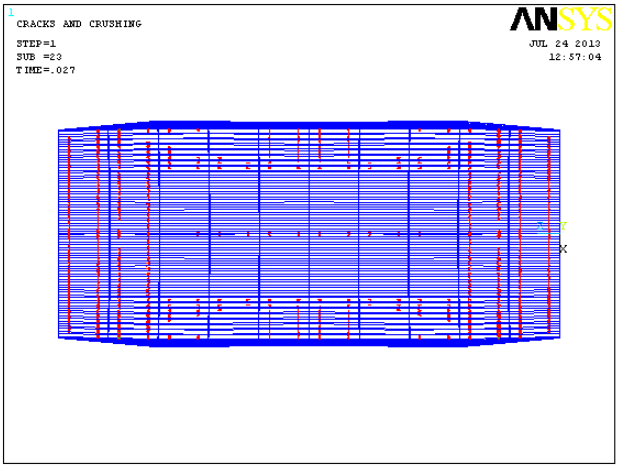

Fig. 21 Crack pattern at failure (top surface) for shell IC-2

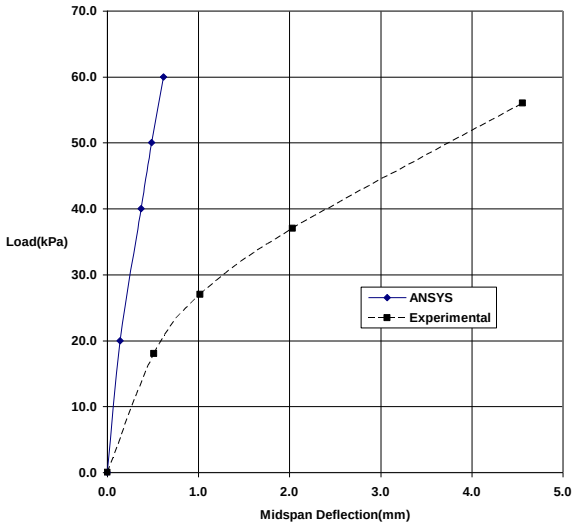

Fig. 22 Load-deflection curve for shell SC-3

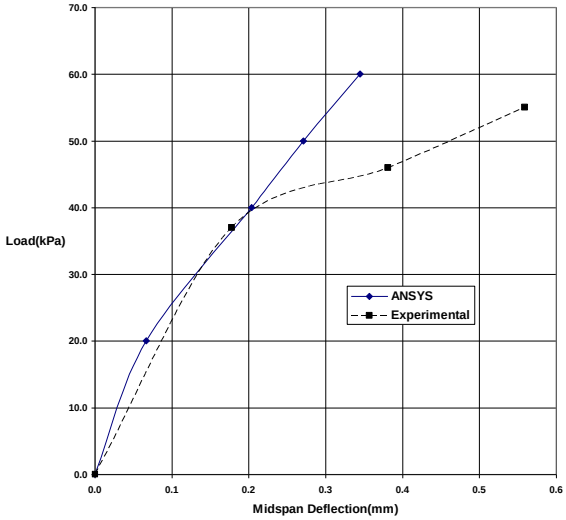

Fig. 23 Load-deflection curve for shell SC-4

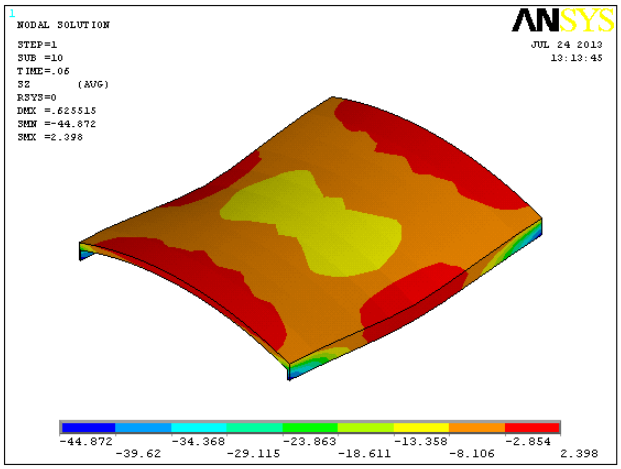

Fig. 24 Longitudinal stress distribution for shell SC-3

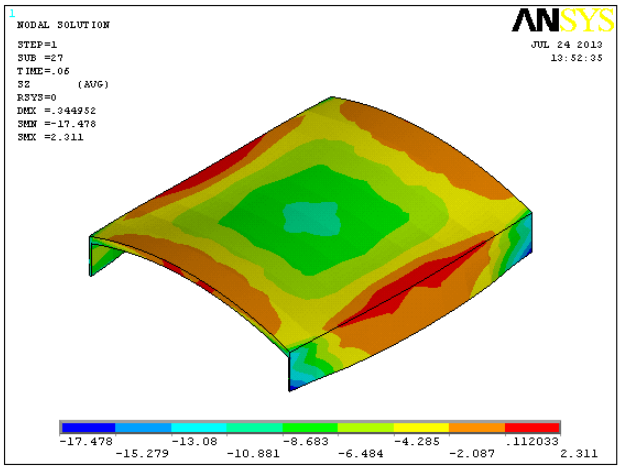

Fig. 25 Longitudinal stress distribution for shell SC-4

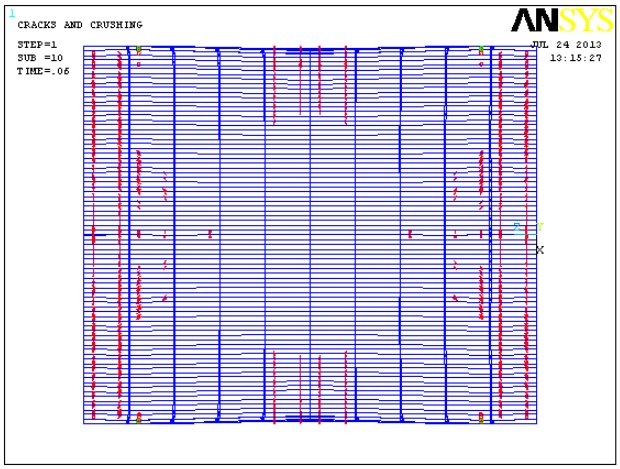

Fig. 26 Crack pattern at failure (top surface) for shell SC-3

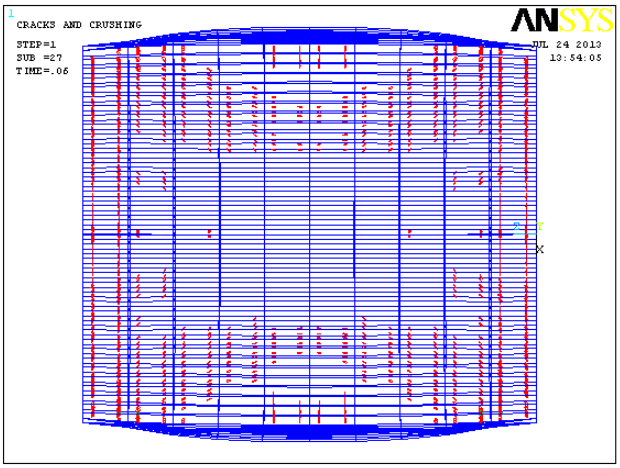

Fig. 27 Crack pattern at failure (top surface) for shell SC-4